Ordered and disordered polymorphs of $Na(Ni_{2/3}Sb_{1/3})O_2$: local structural ordering in honeycomb cathodes for Na-ion batteries

Jeffrey Ma,[a+] Shou-Hang Bo,[a+] Lijun Wu,[b] Yimei Zhu,[b] Clare P. Grey[ac*] and Peter G. Khalifah[ad*]

[a] Chemistry Department, Stony Brook University, Stony Brook, NY 11794, United States

[b] Condensed Matter and Physics and Materials Science Department, Brookhaven National Laboratory, Upton, NY 11973, United States

[c] Chemistry Department, Cambridge University, CB2 1EW, United Kingdom

[d] Chemistry Department, Brookhaven National Laboratory, Upton, NY 11973, United States

KEYWORDS: Na-ion batteries, $Na_3Ni_2SbO_6$, α-$NaFeO_2$, honeycomb ordering, layered oxides, cathode

Abstract:

Na-ion batteries are appealing alternative to Li-ion battery systems for large-scale energy storage applications in which elemental cost and abundance are important. Although it is difficult to find Na-ion batteries which achieve substantial specific capacities at voltages above 3 V (vs. Na^+/Na), the honeycomb-layered compound $Na(Ni_{2/3}Sb_{1/3})O_2$ can deliver up to 130 mAh/g of capacity at voltages above 3 V with this capacity concentrated in plateaus at 3.27 and 3.64 V. Comprehensive crystallographic studies have been carried out in order to understand the role of disorder in this system which can be prepared in both "disordered" and "ordered" forms, depending on the synthesis conditions. The average structure of $Na(Ni_{2/3}Sb_{1/3})O_2$ is always found to adopt an O3-type stacking sequence, though different structures for the disordered ($R\bar{3}m$, #166, $a = b = 3.06253(3)$ Å and $c = 16.05192(7)$ Å) and ordered variants ($C2/m$, #12, $a = 5.30458(1)$ Å, $b = 9.18432(1)$ Å, $c = 5.62742(1)$ Å and $\beta = 108.2797(2)°$) are demonstrated through the combined Rietveld refinement of synchrotron X-ray and time-of-flight neutron powder diffraction data. However, pair distribution function studies find that the local structure of disordered $Na(Ni_{2/3}Sb_{1/3})O_2$ is more correctly described using the honeycomb-ordered structural model and solid state NMR studies confirm that the well-developed honeycomb ordering of Ni and Sb cations within the transition metal layers is indistinguishable from that of the ordered phase. The disorder is instead found to mainly occur perpendicular to the honeycomb layers with a observed coherence length of not much more than 1 nm seen in electron diffraction studies. When the Na environment is probed through ^{23}Na solid state NMR, no evidence is found for prismatic Na environments and a bulk diffraction analysis finds no evidence of conventional stacking faults. The lack of long range coherence is instead attributed to disorder among the three possible choices for distributing Ni and Sb cations into a honeycomb lattice in each transition metal layer. It is observed that the full theoretical discharge capacity expected for a $Ni^{3+}/^{2+}$ redox couple (133 mAh/g) can be achieved for the ordered variant but not for the disordered variant (~110 mAh/g). The first 3.27 V plateau during charging is found to be associated with a two-phase O3 ↔ P3 structural transition, with the P3 stacking sequence persisting throughout all further stages of desodiation.

INTRODUCTION

The development of Na-ion batteries over the past few decades has been limited by the remarkable developments of Li-ion batteries for high power density applications, such as those of the mobile electronics industry [1]. However, Na-ion batteries offer advantages over their Li-ion battery counterparts for emerging large-scale energy storage applications (e.g., grid scale storage) due to the high abundance and low cost of Na. The rich yet relatively unexplored chemistry of Na-ion based electrodes has therefore received renewed interest from the battery community in recent years [2-4]. Although there is no expectation that Na-ion systems will match the energy density of Li-ion systems due to the larger mass, larger size, and less electropositive nature of Na^+ ions, the development of low cost Na-ion systems with high energy densities approaching those of Li-ion systems could have a transformative effect in applications which utilize very large batteries, such as grid scale storage. It is therefore of great interest to investigate design strategies capable of producing Na-ion batteries with maximal energy densities.

Research on Na-ion batteries has focused on two classes of cathode materials with different advantages: layered oxide and complex polyanion frameworks[5-8]. While the layered oxides are generally superior in terms of their specific capacity[9-12], polyanion materials typically can deliver higher operating voltages due to the inductive effect associated with polyanion groups (PO_4^{3-}, SO_4^{2-}, BO_3^{3-}, etc.) [13-15]. Since the complex polyanion groups have a substantially less favorable mass/charge ratio than simple O^{2-} oxide anions, the theoretical capacities of these systems are typically substantially reduced relative to the simpler layered oxide systems. In order to simultaneously achieve both a high specific capacity and a high operating voltage, we have pursued chemical substitutions of classic α-$NaFeO_2$ layered oxides in which a high valence cation is mixed together with the redox active transition metal. It is known that dissimilar cations can form a honeycomb-type order within the octahedral transition metal layers of the α-$NaFeO_2$ structure [16], and we demonstrate that honeycomb ordered $Na(Ni_{2/3}Sb_{1/3})O_2$ has a very favorable energy density due to its high capacity and high voltage.

$Na(Ni_{2/3}Sb_{1/3})O_2$ is structurally related to α-$NaFeO_2$ ($R\overline{3}m$, #166), a structural family which can be considered to be a cation ordered variant of the rock salt structure in which mobile monovalent cations (*A*-cations) and immobile redox-active transition metals (*B*-cations) occupy alternating layers along the $(111)_c$ direction of the basic rock salt cubic lattice (as denoted by the *c* subscript). These compounds have the general stoichiometry of ABO_2. When classified using the nomenclature of Delmas for different layered variants of the general α-$NaFeO_2$ class of compounds [17], $Na(Ni_{2/3}Sb_{1/3})O_2$ is described as having an O3-type structure, where the "O" indicates that the *A* cations (Na) are in an octahedral coordination, and the "3" indicates that the *B* cation layers have a consistent stacking sequence with a period of three layers. The relative offsets of layers of close-packed spheres are commonly given labels of "**A**", "**B**", and "**C**", which correspond to x and y fractional coordinates of (0,0), (2/3, 1/3), and (1/3, 2/3) when described in a trigonal unit cell whose *a*- and *b*-axis lengths are the distance between the centers of neighboring spheres. The compound α-$NaFeO_2$ has lattice parameters of $a = b =$ 3.0251 Å and c = 16.094 Å ($R\overline{3}m$, #166) [18], indicating that the distance between neighboring spheres is a little larger than the ionic diameter of O^{2-} (~2.80 Å). The closely related compound $NaNiO_2$ also has the same O3 stacking sequence, though this is less immediately apparent due to the slight distortion of the basic rhombohedral symmetry that leads to a slightly sheared *C*-centered monoclinic cell with a = 5.33 Å, b = 2.86 Å, c = 5.59 Å and β = 110.3° (*C2/m*, #12) [19]. Even in this monoclinic cell, a translation of about 16 Å in the layer stacking direction still occurs between successive layers of the same *ab* offset and composition (*e.g.*, two neighboring **A** layers hosting Na in $NaNiO_2$ are about 16 Å apart).

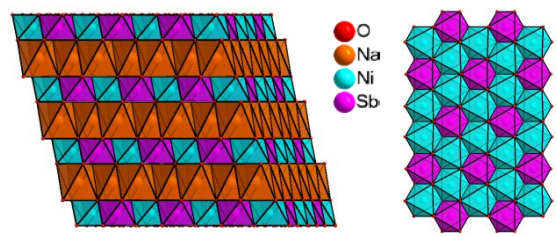

Figure 1. Polyhedral representation the of ideal honeycomb $Na(Ni_{2/3}Sb_{1/3})O_2$ structure viewed parallel (left) and perpendicular (right) to layers.

The substitution of 2/3 of the Ni^{3+} cations in $NaNiO_2$ by Sb^{5+} has two major effects on this structure. First, this reduces the valence of the redox active transition metal to Ni^{2+}, modifying the redox potential and also potentially allowing multivalent redox chemistry ($Ni^{2+} \leftrightarrow Ni^{3+} \leftrightarrow Ni^{4+}$). Second, the large chemical differences between divalent Ni^{2+} and pentavalent Sb^{5+} are expected to give rise to cation ordering on the B-site. $Na(Ni_{2/3}Sb_{1/3})O_2$ has been synthesized and studied by diffraction techniques in a number of previous investigations [16,20-22]. These reports have universally found that $Na(Ni_{2/3}Sb_{1/3})O_2$ possesses an O3 stacking sequence, and generally ascribed a honeycomb type of ordering to the metal layers (each SbO_6 octahedron is surrounded by 6 NiO_6 octahedra, as shown in Fig. 1). The exact degree of ordering appears to be sensitive to synthesis conditions. However a detailed understanding has been elusive since there are only small deviations from the $R\overline{3}m$ symmetry of α-$NaFeO_2$ (which is

expected if the Na/Sb ions are fully randomized over a single crystallographic site), resulting in small changes in the subcell peak positions and intensities. The additional peaks associated with the symmetry-breaking caused by honeycomb cation ordering are typically also weak and can be significantly broadened relative to the subcell peaks. Sometimes superstructure peaks associated with a long range ordering beyond simple cation ordering can also be observed, though the exact nature of the lattice periodicity and structural modifications giving rise to these peaks has not yet been determined[20].

As illustrated in Figure 2, the ideal honeycomb ordering for an O3 layered structure ($R\bar{3}m$ structure) will generate an in-plane (*ab* plane) $\sqrt{3}$a x $\sqrt{3}$a supercell and will typically reduce the lattice symmetry to primitive trigonal ($P3_112$, #151) [23] if no other symmetry-breaking occurs, and to C-centered monoclinic (*C2/m*, #12) if layer shear is also present [24]. These three structure types ($R\bar{3}m$, $P3_112$, *C2/m*) all share the same O3 layer stacking sequence (**ABC**) for the octahedral transition metal layers. The layers are stacked along the *c* direction of the $R\bar{3}m$ and $P3_112$ structures, and the *c** direction of the *C2/m* structure (perpendicular to the *ab* plane of the monoclinic lattice). This difference results in a reduced lattice period in the *C2/m* structure (*c* ~ 5 Å in *C2/m* instead of *c* ~16 Å in $R\bar{3}m$ and $P3_112$) even though the three-layer O3 stacking sequence is maintained in all three space groups. It should be also noted that the lattice origin is shifted in the *C2/m* and $P3_112$ superstructures relative to the $R\bar{3}m$ subcell. When the generic nomenclature of ABO_2 is used to describe the cell contents, the origin is at the *z*-height of the plane of *A* atoms (Na) in the $R\bar{3}m$ subcell, and at that of the *B* atoms (Ni/Sb) in the *C2/m* and $P3_112$ supercells. A more detailed description of the origin choices of the three space groups and their relationships is provided in the Supporting Information (Figure S1).

In this work, the crystal structure of $Na(Ni_{2/3}Sb_{1/3})O_2$ phase and the nature of the Ni/Sb order have been studied through a variety of complementary structural probes, both average (synchrotron X-ray and time-of-flight neutron powder diffraction) and local (pair distribution function studies, electron diffraction, HRTEM imaging, and ^{23}Na solid state NMR structural probes,). The structural changes that can occur in response to variations in the synthesis method and which accompany the desodiation of this phase have been investigated. It is shown that $Na(Ni_{2/3}Sb_{1/3})O_2$ can serve as a high energy density cathode material for Na-ion batteries based on both its high redox potential (plateaus at 3.3 and 3.6 V vs. Na^+/Na from GITT measurements) and high specific capacity (~135 mAh/g, or 0.66 Na/f.u.).

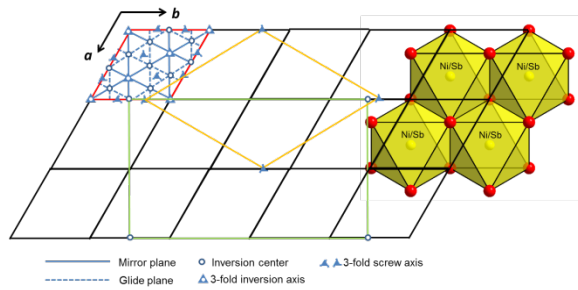

Figure 2. Relationship between the lattices of disordered $Na(Ni_{2/3}Sb_{1/3})O_2$ in the ideal $R\bar{3}m$ α-$NaFeO_2$-type subcell (red), the ideal ordered structure in the trigonal space group $P3_112$ (yellow) and non-ideal ordered monoclinc *C2/m* structure that results from layer shear (green). Superimposed on the lattice are some key symmetry elements, and the positions of transition metal octahedra.

EXPERIMENTAL

Powder synthesis: Low temperature "disordered" $Na(Ni_{2/3}Sb_{1/3})O_2$ was prepared by solid state methods using stoichiometric amounts of sodium carbonate (Na_2CO_3, EMD, 99.9%), nickel hydroxide ($Ni(OH)_2$, Aldrich), and antimony oxide (Sb_2O_3, Alfa Aesar, 99.999%) as precursors. The starting materials were thoroughly ground using an agate motor and pestle, and were then pressed (three tons pressure for two minutes) into a 1/2" dia. pellet . The pellet was placed in a dense alumina crucible and calcined at 750˚C for 1 hour, followed by heating at 850˚C for 1 hour, and 1000˚C for 3 hours, with intermediate grinding and re-pelletizing between each heating inside a box furnace exposed to an ambient air atmosphere. A higher temperature "ordered" $Na(Ni_{2/3}Sb_{1/3})O_2$ sample was prepared using 20% excess Na to compensate for Na loss through volatilization. The "ordered" sample was reacted at 1200˚C for 4 hours after ramping at 200˚C / hr. Other synthesis temperatures and other amounts of excess Na were also investigated using similar protocols.

Electrochemistry: The electrochemical activity of $Na(Ni_{2/3}Sb_{1/3})O_2$ samples was studied using coin cells. A thin film composite cathode was prepared using a 70:20:10 weight ratio of active $Na(Ni_{2/3}Sb_{1/3})O_2$ ceramic, Super P carbon, and polyvinylidene difluoride (PVDF) binder, respectively. The powdered ceramic and Super P were combined and ball milled for 30 minutes in a SPEX SamplePrep8000 Mixer/Mill high-energy ball mill before the PVDF binder was manually ground into the mixture using motor and pestle. N-Methyl-2-pyrrolidone (NMP) was added to this mixture to form a slurry, which was then applied to an aluminum foil and dried at 100˚C overnight. Circular disks of ~14 mm dia. were punched, each with a loading of 5-10 mg of active material. The thin film electrode was assembled into a coin cell in an argon atmosphere glove box. Sodium metal was used as the anode material, and the electrolyte

was 1 M $NaPF_6$ in a 1:1 volumetric mixture of anhydrous ethylene carbonate and dimethyl carbonate (EC:DMC = 1:1). The batteries were allowed to rest for at least 12 hours before cycling.

Cells were galvanostatically tested using an Arbin Instruments battery tester at room temperature. The current density was converted into a C rate based on the theoretical capacity of 199 mAh/g (corresponding to complete Na removal). Cells were typically cycled over a voltage range of 2.5 V to 4.0 V, where the upper voltage limit was chosen based on electrochemical tests which found that charging $Na(Ni_{2/3}Sb_{1/3})O_2$ cathodes to 4.5 V leads to substantial irreversible capacity at high voltages (> 4.0 V) during the first charge cycle (Fig. S2). This irreversible process causes significant capacity fade in subsequent cycles and a large polarization during cycling. It should be noted that persistent differences in the measured charge and discharge capacities have been seen for both the ordered and disordered $Na(Ni_{2/3}Sb_{1/3})O_2$ phases. Since the capacity difference between charge and discharge decreases with increasing current, this difference is ascribed to self-discharge processes associated with the presence of redox shuttling (presumably due to the dissolution of redox active Ni or Sb ions within the electrolyte). The default electrode preparation procedure was therefore modified with the addition of an extra glass fiber separator to minimize the rate of self-discharge.

Testing was also done to verify that the material was fully sodiated prior to the first charge, and that Na loss during electrode preparation is not the cause of the capacity difference between first charge and first discharge cycles. When battery cells of ordered or disordered $Na(Ni_{2/3}Sb_{1/3})O_2$ were cycled starting with a discharge rather than a charge sweep, it was found that these cells had a insignificant first discharge capacity (<1 mAh/g). This indicated that either (1) all Ni is divalent in the pristine compounds and therefore not susceptible to reduction, or (2) all available Na sites are fully occupied, so that no additional Na can be inserted.

Powder diffraction: Laboratory X-ray diffraction measurements for phase identification were carried out on a Bruker D8 Advance laboratory diffractometer (Cu K_α) equipped with a 192-channel Lynx-Eye linear strip detector utilizing a variable slit controlled beam width of 12 mm. For Rietveld refinements, a fixed divergence slit of 0.3° was used instead of the variable slits and a deeper zero-background Si holder with a well depth of 0.30 mm (rather than the typical 0.05 mm) was utilized to minimize preferred orientations of crystallites. Synchrotron X-ray diffraction data was collected at 11BM beamline ($\lambda \sim 0.41$Å) of Advance Photon Source (APS) at Argonne National Laboratory using samples loaded in 0.5 mm dia. Kapton capillaries. Calibration of the instrument for wavelength, detector offsets, and instrument profile shapes was performed with a NIST SRM 660a (LaB_6) standard. Time-of-flight neutron diffraction data was collected at the POWGEN beamline of Spallation Neutron Source (SNS) at Oak Ridge National Laboratory (ORNL) with the samples loaded in 6 mm dia. vanadium cans. All diffraction data sets were analyzed using the TOPAS v4.2 software package.

Neutron total scattering measurements were performed at the NOMAD beamline of the Spallation Neutron Source (SNS) at Oak Ridge National Laboratory (ORNL). Samples were packed into thin-walled quartz capillaries (3 mm dia.). Total scattering data were collected at room temperature under an argon atmosphere. Pair distribution function (PDF) data were processed and reduced using custom IDL scripts to normalize the total scattering data against the V spectrum obtained from a 6 mm diameter V rod, including corrections for absorption, Bragg diffraction, and multiple scattering effects.

Ex situ synchrotron XRD studies were performed on $Na(Ni_{2/3}Sb_{1/3})O_2$ using a series of equivalent batteries that were cycled to different states of charge/discharge. To form the thin film electrode, the powder material and Super P were instead combined and ball milled for 1 hour in a Fritsch Pulverisette 0 vibratory mill (agate mortar and ball, 4" dia.) before the PVDF binder was added. Batteries were then assembled and tested galvanostatically using an Arbin battery cycler at constant current of C/50. Cells were then disassembled, in an argon glove box with the cathode material scraped off and washed thoroughly using DMC. The obtained material was then packed into 0.5 mm Kapton tubes for synchrotron X-ray diffraction measurements.

Transmission electron microscopy: TEM analyses were performed using a JEM-ARM200F microscope operating at 200 kV. The as-synthesized particles were mechanically ground to create small isolated crystallites (< 100 nm) suitable for analysis. The ground powder was then ultrasonically dispersed in alcohol within a small glass bottle and added dropwise onto a lacey carbon grid for analysis.

Solid state NMR: ^{23}Na ($S = 3/2$) magic angle spinning (MAS) nuclear magnetic resonance (NMR) measurements were performed with a 1.3 mm HX probe (Ago Samoson), using a Tecmag 200 MHz spectrometer (4.7 T magnetic field). The Larmor frequency of ^{23}Na is 52.78 MHz. A rotor-synchronized spin echo sequence ($\pi/2$-τ-π-τ-acquisition) was utilized, with a spinning speed of 50 kHz. A pulse width of 1.1 μs ($\pi/2$) was used. A recycle delay of 100 ms was used for typical data collections, as the T_1 relaxation time was determined to be less than 10 ms. Scans with a much longer recycle delay were also collected on selected samples to test for the presence of diamagnetic impurities. A NaCl solution (1 M) was used as an external chemical shift reference (0 ppm). The collected spectra were analyzed using the DMFit software

package[25] to extract C_Q (quadruple coupling constant) and η (asymmetry parameter) for ^{23}Na resonances.

RESULTS AND DISCUSSION

Ordered and disordered $Na(Ni_{2/3}Sb_{1/3})O_2$ polymorphs

During initial attempts to prepare $Na(Ni_{2/3}Sb_{1/3})O_2$, it was observed that two different types of characteristic powder X-ray diffraction patterns could be obtained, depending on the synthesis conditions. At lower temperatures such as 1000 °C, many fewer low angle diffraction peaks were observed (Fig. 3) and all of the sharp peaks in the diffraction pattern could be effectively indexed with a unit cell of $a = b = 3.06$ Å and $c = 16.05$ Å using the $R\bar{3}m$ space group expected for an α-$NaFeO_2$ subcell. The small *a*-axis length is the translational period that is equal to the distance between the centers of nearest neighbor BO_6 octahedra in the ABO_2 nomenclature, and thus indicates that on average, the Ni^{2+} and Sb^{5+} cations must be disordered. This low temperature polymorph is therefore considered to be "disordered", and will be referred to as D-$Na(Ni_{2/3}Sb_{1/3})O_2$.

In contrast, when the synthesis was carried out at a temperature of 1200 °C, a number of additional low angle diffraction peaks were found and these peaks could be readily indexed with a $\sqrt{3}$ x $\sqrt{3}$ x 1 trigonal supercell of the low temperature rhombohedral cell (Fig. 3). These increased lattice parameters in the *ab* plane are characteristic of Ni/Sb ordering, and this pattern is therefore ascribed to an "ordered" polymorph of $Na(Ni_{2/3}Sb_{1/3})O_2$, which is denoted O-$Na(Ni_{2/3}Sb_{1/3})O_2$. It should be noted that in addition to increasing the reaction temperature to 1200 °C, it was also necessary to add excess Na (typically 20%) before the "ordered" XRD pattern could be observed. In addition to having extra diffraction peaks, the ordered phase shown in Fig. 3 also has reduced peak widths relative to the disordered phase, a difference which was found to be primarily due to a reduction in strain in whole-pattern fitting. Some XRD patterns for additional synthesis conditions and their tendency for ordering are given in Fig. S3.

Deeper insights into the structures of these two polymorphs were obtained by the combined Rietveld refinement of synchrotron X-ray and time-of-flight neutron diffraction data, starting with the disordered phase, D-$Na(Ni_{2/3}Sb_{1/3})O_2$ (Fig. 4). The use of neutron diffraction data gives enhanced sensitivity to the lighter elements in the structure (O and Na), as can be seen in the relative scattering lengths for these four elements (in fm, Na 3.63; Ni 10.3; Sb 5.57; O 5.803). Excellent fits to both the X-ray and neutron diffraction data can be simultaneously obtained using a common disordered structural model with the space group $R\bar{3}m$ (#166), with cell dimensions of $a = b = 3.06253(3)$ Å and $c = 16.05192(7)$ Å. In this simple α-$NaFeO_2$ structural model, there are only three crystallographic sites: one for the *A* cation (Na), one for the B cations (mixed Ni/Sb with fractional occupancies of 2/3 and 1/3, respectively), and one for the O anions. Full structural information is provided in Tables S1-3.

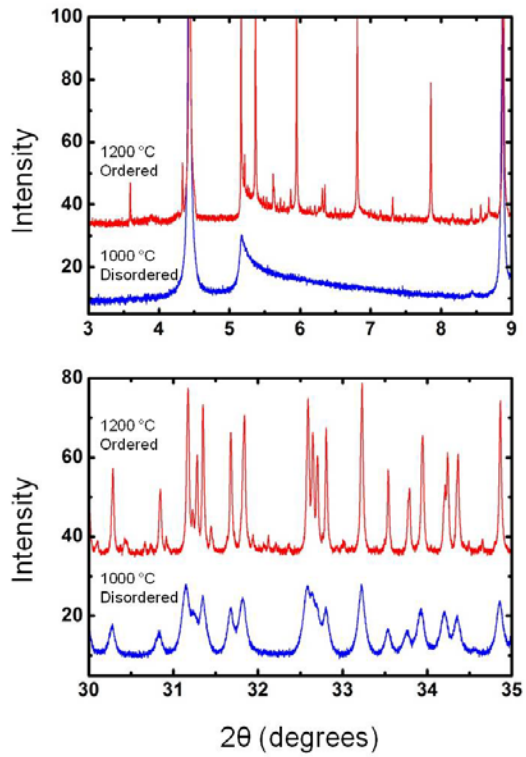

Figure 3. Low angle (top) and high angle (bottom) synchrotron X-ray diffraction data (11-BM, λ = 0.4137 Å) for disordered and ordered $Na(Ni_{2/3}Sb_{1/3})O_2$ synthesized at 1000 °C and 1200 °C, respectively. Intensities are displayed on a square root scale.

While this structural model very effectively describes the intensity of the sharp Bragg peaks, it can be seen that there are two additional broad peaks at $d = 2.3$ Å and $d = 4.6$ Å that are not expected to be present in the simple $R\bar{3}m$ model (Fig. S4). Although these peaks cannot be assigned integer Miller indices in the simple $R\bar{3}m$ cell, the two peaks can be indexed as the 010_P and 020_P reflections of the $\sqrt{3}$ x $\sqrt{3}$ primitive trigonal supercell ($P3_112$), where the "P" indicates that the indices correspond to the primitive trigonal supercell rather than rhombohedral subcell. However, none of the other peaks that should occur in this supercell are observed. This suggests that the $R\bar{3}m$ cell is still the most appropriate space group for describing the translation symmetry of D-$Na(Ni_{2/3}Sb_{1/3})O_2$, and that the two extra broad peaks are indicative of local order that persists across a short length scale rather than exhibiting full three-dimensional (3D) long range order. Furthermore, these two peaks both have a Miller index

of L = 0, suggesting that the local ordering originates from two-dimensional (2D) in-plane ordering which is presumably associated with the development of the $SbNi_6$ honeycomb ordering, and that there is no coherence in the positions of Ni and Sb between successive octahedral layers stacked along the *c*-axis.

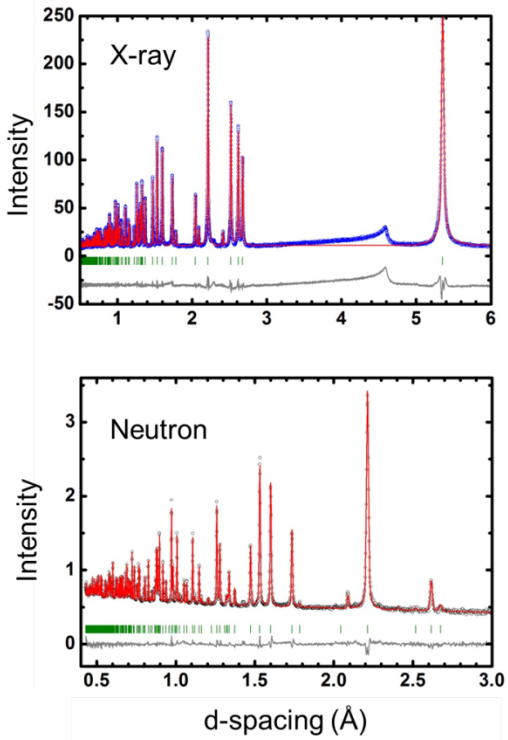

Figure 4. Combined synchrotron X-ray (top) and time-of-flight neutron (bottom) refinement of 1000 °C disordered D-$Na(Ni_{2/3}Sb_{1/3})O_2$ in space group $R\bar{3}m$, with the tick marks indicating peak positions, the modeled intensity shown in red, and the difference pattern shown in gray. A minor impurity of 1 wt% NiO was included in the fit, though tick marks for this phase are not shown. Intensity is displayed on square root scale. Additional plots of the data are given in Fig. S6 of the Supporting Information.

Electron diffraction studies were carried out to better understand the partial ordering of Ni and Sb cations hinted at by powder diffraction studies of the disordered sample, D-$Na(Ni_{2/3}Sb_{1/3})O_2$. The large secondary particles (10 – 20 μm, Fig. S5) of this phase were mechanically separated by grinding, and were found in TEM studies to primarily consist of hexagonal plates that are a few microns in width and 100 - 300 nm in thickness (Figure 5a). The plate normal corresponds to the $[001]_R$ direction ("R" indicates the indices correspond to the rhombohedral cell), and therefore reflects the stacking of octahedral layers along the *c*-axis direction. Electron diffraction patterns were collected both with the beam parallel to the $[001]_R$ direction (Figure 5b) and perpendicular to the $[001]_R$ direction (Figure 5c/d). In all electron diffraction patterns collected in $[001]_R$ zones, the superstructure reflections corresponding to the larger primitive trigonal cell could be observed, indicating that the $R\bar{3}m$ structure is entirely inadequate for describing the structure of "disordered" D-$Na(Ni_{2/3}Sb_{1/3})O_2$ on a local scale. The $\sqrt{3}$ x $\sqrt{3}$ x 1 $P3_112$ trigonal supercell which was used to index the laboratory XRD patterns of the "ordered" sample can be used to completely index all observed diffraction spots in the electron diffraction pattern of $[001]_R$ zones (labels for both cells are marked in Figure 5b), though we note that our detailed study of synchrotron diffraction data indicates the true symmetry of O-$Na(Ni_{2/3}Sb_{1/3})O_2$ is very slightly distorted to monoclinic. The observation of the electron diffraction superstructure for D-$Na(Ni_{2/3}Sb_{1/3})O_2$ indicates that there are very strong ordering preferences for Ni and Sb even at the lowest synthesis temperatures explored in this study, and suggests that the in-plane honeycomb ordering is probably fully developed for the "disordered" phase.

Although the *ab*-plane ordering of Ni and Sb is well-developed in the disordered phase, there is no evidence of coherence in the *c*-axis direction. This can be explicitly seen in the rods of diffraction intensity observed for the $[100]_P$ zone axis (Fig. 5d). These rods run parallel to the $[001]_P$ direction, and are found at positions such as $[01L]_P$ and $[02L]_P$ that are allowed in the primitive trigonal superstructure but which are forbidden in the rhombohedral subcell. The absence of extra intensity at the Bragg positions which lie on these rods of diffraction suggest that they originate from order which is purely two-dimensional, and lacks three-dimensional coherence. This lack of coherence can be clearly seen in the HRTEM image shown in Figure 5e, which illustrates the abundance of stacking faults in the *c*-axis direction (vertical axis of figure) even over a length scale of a few nm which is short relative to the length of the minimum layer repeat distance in $Na(Ni_{2/3}Sb_{1/3})O_2$ of 5 Å. These stacking faults are believed to be the source of additional features observed in both electron diffraction patterns (weak spots indicative of a doubled c-axis periodicity in Fig. 5c and the twinning observed in Fig. 5f) and in synchrotron diffraction data for the O-$Na(Ni_{2/3}Sb_{1/3})O_2$ phase (Fig. S7) which shows weak peaks at the positions expected for 4*c* and 9*c* superstructures (discussed later).

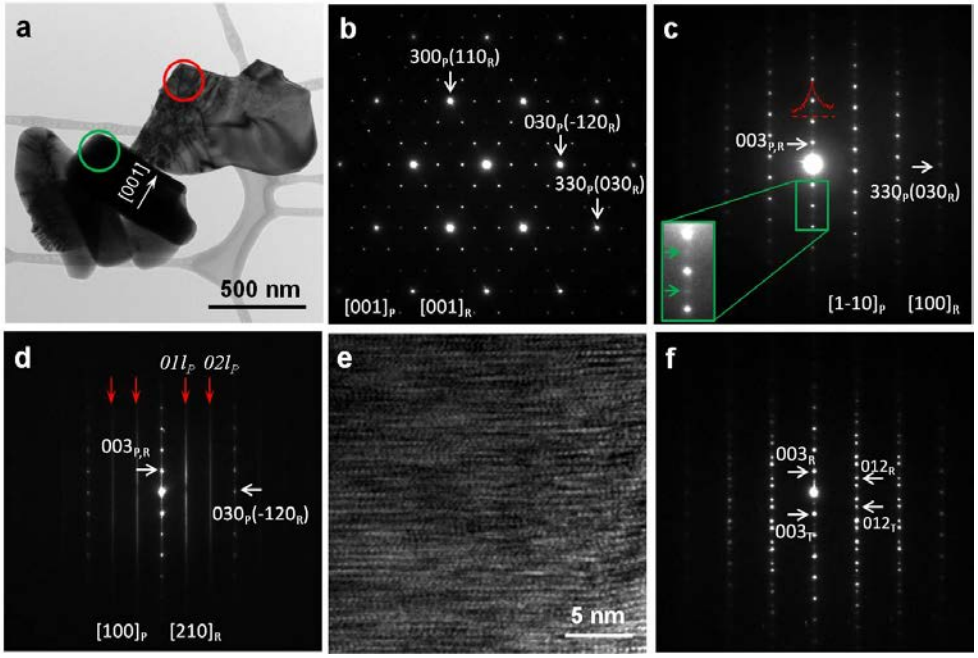

Figure 5. (a) Morphology of D-Na($Ni_{2/3}Sb_{1/3}$)O_2 particles. (b) The $[001]_R$ electron diffraction pattern (EDP) from the region marked by a red circle in (a), a pattern which can be more completely indexed by a $P3_112$ primitive trigonal (P) superstructure than the simple disordered rhombohedral cell (R). (c,d) EDPs taken from the particle marked by green circle in (a). (c) The EDP from $[1\text{-}10]_P$ zone, with an embedded intensity profile (red) from a scan across the red dashed line. Inset in (c) shows magnified and contrast enhanced spots from a selected area (green box), highlighting the superlattice observed at L = 3/2 positions between the strong reflections from the c = 16 Å $R\bar{3}m$ subcell. (e) HRTEM image from an $[100]_R$ zone, with the $[001]_R$ direction oriented vertically allowing the abundant stacking faults in this direction to be seen. (f) An EDP showing the commonly observed twin pattern (subscript T denotes reflections associated with the twin domain) that corresponds to a ~~rotation~~ reflection twin with ~~about~~ the ~~-~~(001)$_R$ twin plane~~direction~~ (measured on separate particle). The observed twinning is common but not universal for every particle that was studied.

Pair distribution function (PDF) studies offer the opportunity to probe the local structure of the entire sample, rather than just the small subset of regions explored in electron microscopy experiments. Neutron PDF data were used to probe the nature of the disorder in a sample of D-Na($Ni_{2/3}Sb_{1/3}$)O_2. Fits to the PDF data were carried out using both the random $R\bar{3}m$ subcell structural model (Figure 6, top) and the ordered $P3_112$ supercell structural modal (Figure 6, bottom). Both models essentially give the same quality of fit over long range distances of 10 – 30 Å, with the ordered model having only a marginally lower R-value (0.16 vs. 0.17) despite using substantially more refined parameters (22 vs. 7). However, there is a large improvement in the quality of fit to the short range correlations (1.7 – 10 Å) when the ordered $P3_112$ structure (R_w = 0.11) is used instead of the disordered $R\bar{3}m$ structure (R_w = 0.15). These data unambiguously indicate that the "disordered" D-Na($Ni_{2/3}Sb_{1/3}$)O_2 sample has well-developed honeycomb order on the local scale, and that it is only the presence of abundant defects prevents this order from being observed in the bulk X-ray diffraction patterns. The TEM results suggest that the dominant defects are stacking faults, and they clearly show that c-axis stacking faults are abundant enough to cause the effective randomization at distances beyond 10 Å.

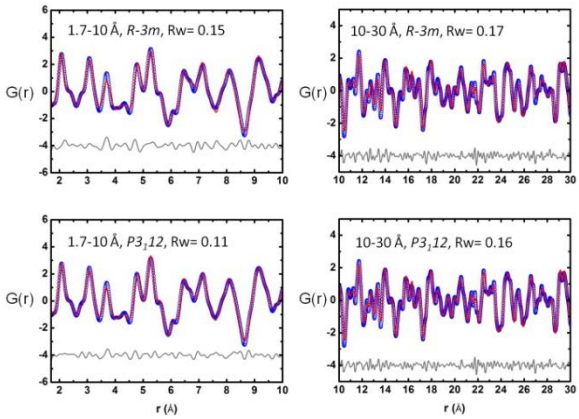

Figure 6. Fits of neutron PDF data for a disordered D-Na($Ni_{2/3}Sb_{1/3}$)O_2 sample over short (left) and longer (right) length scales using either the disordered $R\bar{3}m$ subcell (left) or the ordered $P3_112$ supercell. The use of the honeycomb-ordered $P3_112$ supercell substantially improves the fit

quality at distances below 1 nm, but has a negligible effect at longer distances.

The structure of the ordered O-Na($Ni_{2/3}Sb_{1/3}$)O_2 can be determined much more simply than that of the disordered polymorph since there is a single structure which is relevant at all length scales. The combined Rietveld refinement of synchrotron X-ray and time-of-flight neutron diffraction data (Figure 7) was used to determine this structure. Although both the laboratory X-ray diffraction data and the electron diffraction data for this ordered phase could be effectively indexed using the ideal trigonal $P3_112$ superstructure, high resolution synchrotron diffraction data clearly indicates that there are small but significant deviations from the ideal trigonal symmetry (Figure S8). Large improvement in the modeling of peak shapes is achieved when a lower symmetry monoclinic space group is used, indicating that the 3_1 screw axes of the archetypical rhombohedral cell are not retained when Ni/Sb ordering is present, and that a slight degree of shear between successive layers is induced by the ordering. The refined monoclinic lattice parameters are a = 5.3046(1) Å, b = 9.1843(2) Å, c = 5.6274(1) Å and β = 108.2797(2)°. The crystal structure of O-Na($Ni_{2/3}Sb_{1/3}$)O_2 was refined using space group *C2/m* (#12), which was chosen because it preserves all of the symmetry elements of $R\bar{3}m$ subcell that do not violate the lower lattice symmetry, and this space group has previously been used to model the closely related honeycomb ordered compound, Li_2MnO_3 [26]. In the *C2/m* space group, two atomic sites are associated with each atomic environment (Na, Ni/Sb and O), and the multiplicity of these paired sites each have the same 2:1 ratio, as can be seen in the tabulated crystallographic parameters (Tables S4-6).

Although the *C2/m* monoclinic structure is very effective in modeling the scattering at the Bragg diffraction peaks associated with the honeycomb ordering of Ni and Sb cations within the O3 structure of O-Na($Ni_{2/3}Sb_{1/3}$)O_2, the high intensity synchrotron data exhibits some additional weak peaks which are unindexed by this unit cell (Figure S7), as has been previously noted [20]. Many of these extra peaks occur at large *d*-spacings, indicating that they are associated with a large period translation. These peaks can be effectively indexed using either a 4*c* or 9*c* superstructure, as can be clearly seen in Pawley fits to the synchrotron diffraction data (Fig. S7). Based on the minimal intensity of these reflections, it is expected that these larger periods are associated with specific stacking alternatives to the basic 3-layered O3 repeat of the $R\bar{3}m$ subcell that infrequently occur and represent metastable rather than thermodynamically stable packing motifs. As such, it is presently expected that the *C2/m* monoclinic structure is still the best choice for structural refinements of powder diffraction data.

One effective manner of probing the presence of honeycomb ordering on the local scale is through ^{23}Na solid state NMR experiments, which probe resonances

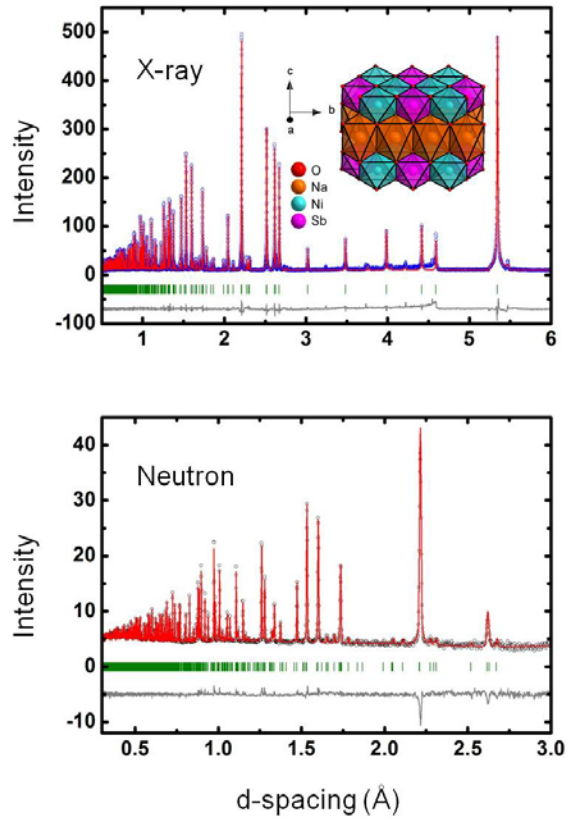

Figure 7. Combined Rietveld refinement of synchrotron X-ray and time-of-flight neutron diffraction data for ordered O-Na($Ni_{2/3}Sb_{1/3}$)O_2 synthesized at 1200 °C with 20% excess Na. A minor (< 1 wt%) Na_3SbO_4 impurity was included in the refinement, but its tick marks are not shown in these plots. The intensity axis is displayed on square root scale. Additional plots of the data are provided in Fig. S9.

of this quadrupolar nucleus (S = 3/2). The ^{23}Na NMR shift is primarily sensitive to its local environment, which in this case corresponds to the six nearest neighbor octahedral sites and the pattern by which Ni and Sb are arranged over these six octahedra. Differences in the ^{23}Na local environment will be reflected in the measured values of C_Q (quadrupolar coupling constant) and η (asymmetry parameter). The ^{23}Na NMR spectrum of the ordered sample (Figure 8) has two resonances (hyperfine shifts, 1625 ppm and 1465 ppm) as well as their spinning sidebands (marked by asterisks). Although a third measured resonance at 4384 ppm (Fig. S10) has previously been ascribed to this compound [22], this signal is purely external as it arises from the Cu foil employed in the NMR probe. Both the Na1 and Na2 resonances display the classical lineshapes for a quadrupolar nucleus, as expected for ^{23}Na.

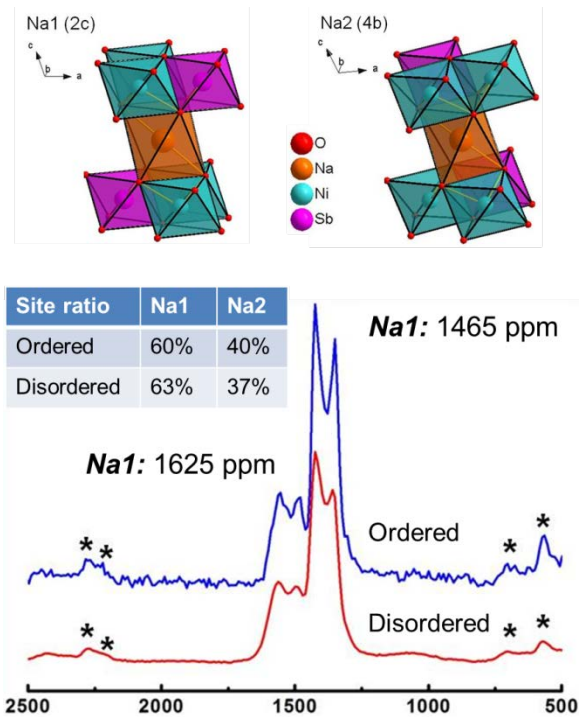

Figure 8. ^{23}Na NMR spectra of ordered and disordered $Na(Ni_{2/3}Sb_{1/3})O_2$. Spinning sidebands are marked by asterisks. Site ratios were determined from integrated peak intensities. The local environment of the two Wykoff sites for Na1 (2c) and Na2 (4h) in the monoclinic C/2m structure of the ordered phase are shown, with the 2c site having a higher site symmetry (2/m) than the 4h site (2).

When explicitly modeled, these two ^{23}Na resonances are found to have similar values of C_Q (~3 MHz) and η (~0.3), suggesting the corresponding Na sites possess very similar local environments. In the ordered structure, the observed intensity ratio (60:40) of the two Na resonances is close to 2:1 which is consistent with the expectations for the two different Na sites (4h and 2c sites) of an ideal honeycomb ordered *C2/m* structure. The large NMR shifts (>1000 ppm) of these two resonances are primarily induced by the hyperfine interaction between Na and the unpaired electrons of Ni^{2+} through intervening O atoms. The relatively small shift difference (160 ppm) is caused by the variations in the ^{23}Na second-order quadrupolar interaction, which reflects the different point group symmetries of these two sites. As illustrated in Figure 8, the lower symmetry 4h Wykoff site of Na2 has only a 2-fold rotation axis (parallel to the *b*-axis), while the higher symmetry 2c Wykoff site of Na1 has a site symmetry of 2/m (due to the inversion center at the Na site and the additional mirror plane perpendicular to the *b*-axis that this generates). As long as the stacking faults maintain the octahedral environment of Na ions, they will change neither the types nor the abundance of local environments in which the Na ions can be found. In contrast, defects in the honeycomb ordering of Ni and Sb ions would be expected to result in different local environments for Na ions (such as those that contain 3 or 5 rather than 4 Ni nearest neighbors) and should generate new resonances in the NMR spectrum. The absence of such resonances indicates that the honeycomb ordering is very robustly obeyed in this ordered structure.

When the NMR spectrum of the disordered phase is compared to that of the ordered phase, no substantive differences are observed in the position, number, or intensity ratio of the ^{23}Na resonances. This strongly suggests that in-plane honeycomb ordering is fully developed even in D-$Na(Ni_{2/3}Sb_{1/3})O_2$. The diffraction, TEM, PDF, and NMR analysis all are fully consistent with the conclusion that honeycomb order is robustly developed for both the ordered and disordered forms of $Na(Ni_{2/3}Sb_{1/3})O_2$, and that the primary difference between different preparations is the frequency of stacking faults perpendicular to the octahedral layers (*ab* plane).

Nature of the stacking faults

To better understand the nature of the stacking faults in this system, a detailed structural analysis of D-$Na(Ni_{2/3}Sb_{1/3})O_2$ was carried out. One of the most common stacking faults observed in close-packed layered structures is the shear of layers which modifies the stacking sequence. For instance, a shear of the **C** layer in an **ABC** stacking sequence could lead to an **ABA** domain, which generates a hexagonal-close-packed stacking fault in what would otherwise be an exclusively cubic-close-packed structure. In the case of O3-stacked structures such as the present $Na(Ni_{2/3}Sb_{1/3})O_2$ compound, prismatic stacking faults (such as **AA**) which result in different environments for Na should also be considered to be possible as this coordination environment is thermodynamically stable for some compositions (such as those with the P3 stacking sequence). The local environment of Na is very different in trigonal prismatic and octahedral geometries. The fact that we observed only the expected octahedral Na resonances in NMR studies (Fig. 8) strongly suggests that prismatic local environments are rare. It is thought that at most 5% prismatic Na could be present but undetected in D-$Na(Ni_{2/3}Sb_{1/3})O_2$, based on the estimated detection limit of the present NMR data.

Since the NMR data showed no evidence for Na atoms in prismatic coordination environments, modeling efforts to identify the nature of the stacking faults in D-$Na(Ni_{2/3}Sb_{1/3})O_2$ were constrained to only probe defects in which the Na ions are octahedrally coordinated, and in which the Ni/Sb ions also remain octahedrally coordinated. All possible stacking variants which obeyed these rules were then explicitly generated for a $\sqrt{3}a$ x $\sqrt{3}a$ x 6*c* supercell of the α-$NaFeO_2$ structure

type with c ~ 32Å containing 6 Na layers, 6 Ni/Sb layers, and 12 O layers. This produced more than 2000 possible stacking sequences, though it is noted that a number of these are topologically equivalent. When Rietveld refinements were carried out for all of these stacking variants (Fig. S11), none of the alternate stacking sequences were found to improve the fit quality relative to that for the base O3 structure type.

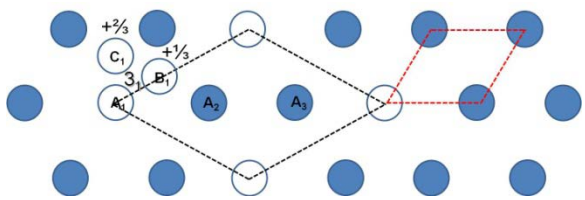

Figure 9. Schematic illustration of a close-packed Ni/Sb layer and its stacking. The base $R\bar{3}m$ symmetry (1a x 1a) subcell is shown in red. The honeycomb ordering of Ni and Sb produces the $\sqrt{3}a$ x $\sqrt{3}a$ supercell indicated by black lines. This type of ordering creates 3 different potential positions in each Ni/Sb layer, such as the $\mathbf{A}_1$, $\mathbf{A}_2$ and $\mathbf{A}_3$ positions in the **A** layer drawn above. When Sb occupies the $\mathbf{A}_1$ position in the **A** layers, Sb should also be found at the $\mathbf{B}_1$ position in the **B** layer (~5 Å above A) and the $\mathbf{C}_1$ position in layer **C** (~10 Å above A) as these sites are related by a 3-fold screw axis (3_1) in the ideal O3 stacking sequence.

This observation that the O3 stacking sequence is very well preserved needs to be reconciled with the observed the HRTEM imaging data, which indicate that a stacking fault occurs almost every 10 Å along the c-axis direction. Taken together, the data suggest that the stacking faults occur not from alternate arrangements of the close-packed oxygen anion positions, but rather from disorder of the relative positions of the Sb and Ni cations in the honeycomb layers. In any given honeycomb layer with cations exclusively situated in the **A** type of octahedral voids, there are three possible positions for the Sb cations at the center of the honeycombs, labelled as $\mathbf{A}_1$, $\mathbf{A}_2$ and $\mathbf{A}_3$ in Figure 9. In this figure, the Sb cations (open circles) are placed on the $\mathbf{A}_1$ site while the Ni cations must occupy the remaining two sites ($\mathbf{A}_2$ and $\mathbf{A}_3$). The choice of the Sb site positions in successive layers should ideally be determined by the space group of the average structure. For example, the 3_1 screw axis of space group $P3_112$ structure results in the Sb cations in subsequent layers being placed in the specific $\mathbf{B}_1$ and $\mathbf{C}_1$ sites indicated in Fig. 9. However, if the Sb cations in those layers were to instead occupy the alternate "2" or "3" sites in which Ni should reside, this would lead to stacking faults and the average symmetry of the lattice being raised to the $R\bar{3}m$ symmetry of α-$NaFeO_2$. Thus the higher apparent symmetry of D-$Na(Ni_{2/3}Sb_{1/3})O_2$ relative to O-$Na(Ni_{2/3}Sb_{1/3})O_2$ results from Ni/Sb orientational disorder, rather than from violations of the preferred O3 stacking sequence of close-packed layers. In contrast, it is anticipated that the 4c and 9c superstructures of ordered O-$Na(Ni_{2/3}Sb_{1/3})O_2$ result from alternate close-packed stacking motifs (which are often stabilized by elevated temperatures) as these represent common stacking sequences in other compounds with mixed-close-packed motifs (typically based on **hchc** and **hhchhchhc** alternations between hexagonal, **h**, and cubic, **c**, stackings of close-packed layers), though this hypothesis has not yet been explicitly tested against the available diffraction data and is beyond the scope of the present work.

Electrochemistry of $Na(Ni_{2/3}Sb_{1/3})O_2$

Given the substantial differences in their diffraction patterns, the electrochemical performance of ordered and disordered $Na(Ni_{2/3}Sb_{1/3})O_2$ as cathodes in Na-ion batteries were separately investigated. All C-rates were calculated assuming that the theoretical capacity of this system is 199 mAh/g (full Na removal), though it should be noted that this value requires the assumption of two-electron redox processes for Ni and that the theoretical capacity is reduced to 133 mAh/g (2/3 Na removal) if only one-electron Ni redox processes are considered. During galvanostatic testing, these two phases were both cycled between 2.5 and 4 V in a 1M $NaPF_6$ electrolyte dissolved in an EC/DMC mixture (1:1 by volume), starting with a charge cycle to remove Na ions. The results of these tests are shown in Figure 10. As previously reported[22,27], both compounds exhibit two well-defined plateaus on charge and discharge, with average voltages of about 3.3 and 3.65 V, respectively. The first charge plateau at 3.3 V is considerably wider than that of the second plateau, and it appears that the system may have one or more additional electrochemical processes that occur at voltages intermediate to these two plateaus.

There are a number of promising characteristics of these cycling profiles. In particular, the discharge voltage is both high and flat over an extended range of capacities. Up to ~130 mAh/g can be delivered at voltages of 3 V or higher, with an average voltage of about 3.4 V vs. Na^+/Na. While it is common to find α-$NaFeO_2$ type phases such as $NaNiO_2$ [28] which can have an initial discharge voltage approaching 3 V, the voltage profile of these phases are either strongly sloping or exhibit a staircase pattern, and rarely exceed a discharge capacity of 100 mAh/g above 3 V [29-33]. The sloping (or staircase) behavior of those phases is attributed to a multitude of intermediate phases with different types of Na-ion ordering. The compound $Na(Ni_{2/3}Sb_{1/3})O_2$ is therefore remarkable in being dominated by only two well-defined electrochemical features, whose structural origin will be discussed later.

In addition to having a high power density, these $Na(Ni_{2/3}Sb_{1/3})O_2$ electrodes can be cycled reversibly, demonstrating their suitability for secondary (rechargeable) batteries. Over 30 cycles, the capacity retention at a C/50 rate is about 90% for the ordered phase and 70% for the disordered phase. This is a reasonable degree of capacity retention for a system whose device construction has not been extensively optimized. While good performance is obtained at slow rates of charge/discharge, it is clear that this system is ineffective at higher rates. A large and abrupt loss of capacity is seen to occur sometime in the first 30 cycles for disordered systems cycled at C/5 or faster, and for ordered systems cycled at rates of C/20 and faster. Since the observed capacity at rates below these thresholds is not strongly affected by rate and since the decay of capacity is non-monotonic for some cycle rates, it is expected that there is a high-barrier nucleation (or other) process that is limiting the rate performance of these systems. This is consistent with the ~0.2 V overpotential (relative to subsequent cycles) needed to initiate cycling in the first charge cycle of O-$Na(Ni_{2/3}Sb_{1/3})O_2$. It is not yet known if the improved rate performance of D-$Na(Ni_{2/3}Sb_{1/3})O_2$ is due to the disorder in the system, or the smaller particle sizes that result from the lower synthesis temperature of this preparation (1200 °C vs. 1000 °C). For either of these origins, there are methods which may be effective in allowing the system to function at higher rates (high-energy ball milling, chemical substitution, etc.). Electrochemical tests were also carried out over a narrower voltage range (2.5 to 3.4 V) to determine whether improved capacity retention would occur when only the lower redox plateau of 3.3 V was utilized. Improvements in lifetime were at best marginal (Fig. S12), suggesting that that there is no advantage to limiting the voltage accessible capacity range in this manner. The flat plateaus during cycling remain during testing at higher C rates (Fig. S13), suggesting that the primary limitations are kinetics and can likely be overcome by improved battery fabrication. Indeed, highly improved rate performance (~100 mAh/g capacity at 2C) and capacity retention (70% retained over 500 cycles at 2C) have been very recently reported[22] using a slightly different $Na(Ni_{2/3}Sb_{1/3})O_2$ cathode formulation which varied from the present work in both the ceramic synthesis temperature (900 °C) and in the electrolyte used during testing (diethyl carbonate instead of dimethyl carbonate). It can be seen from SEM data (Fig. S5) that the nanoscale primary particles in the present work are highly fused typically forming large (> 10) and very dense secondary particles in a manner reminiscent of partial melting or flux-aided growth. This morphology is very unfavorable for battery performance, and it is therefore expected that synthesis methods which avoid melting the Na_2CO_3 starting material (m.p. ~ 850 °C) may dramatically enhance battery performance of the resulting product.

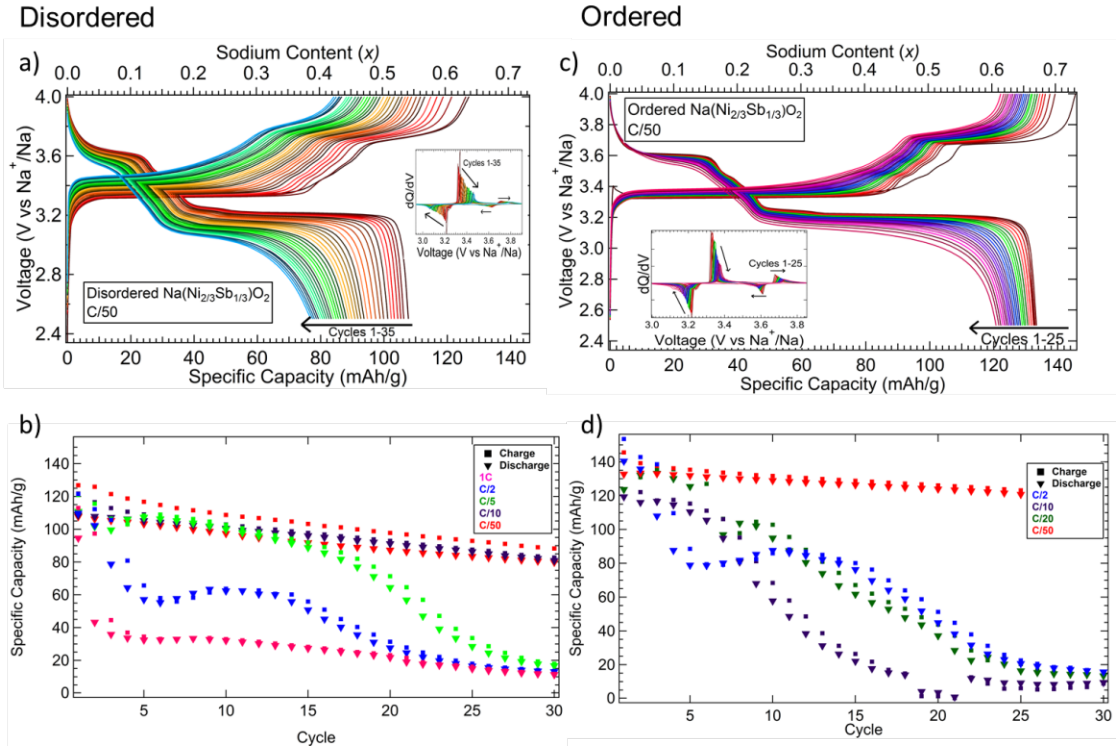

Figure 10. Cycling profiles (a,c) and rate performance (b,d) of the disordered and ordered $Na(Ni_{2/3}Sb_{1/3})O_2$.

Although divalent nickel ions are known to be capable of carrying out 2-electron redox processes (2+ ↔ 4+) in other structurally related layered battery systems[34,35], the maximum specific capacity achieved for the present system is just over 130 mAh/g. This very closely corresponds to the 133 mAh/g expected capacity for an one-electron redox process of Ni (2+ ↔ 3+), and suggests that Ni^{4+} is not accessible in the present system below 4 V. This is perhaps closely related to the presence of Sb^{5+} in the honeycomb-ordered lattice, as the strong Coulombic repulsions that would occur between Ni^{4+} and Sb^{5+} cations in very close proximity in neighboring octahedra (~3.1 Å separation) may prevent this valence state of Ni from being accessed below 4 V. A recent XPS study has found no evidence for the formation of Ni^{4+} at the surface of $Na(Ni_{2/3}Sb_{1/3})O_2$ in fully charged cathodes[22].

While the presence of Sb^{5+} is hypothesized to limit the accessible specific capacity of $Na(Ni_{2/3}Sb_{1/3})O_2$, the same Coulombic repulsions are also expected to raise the redox voltage in this compound as they more strongly destabilize the oxidized state than the reduced state of nickel. Gavanostatic testing of the closely related compound $Na_{2/3}(Ni_{2/3}Te_{1/3})O_2$ has been recently reported [36], and this phase exhibits even higher discharge voltages of 4 V on average, as might be expected from the stronger repulsions associated with the higher valence of Te^{6+}. This effect therefore appears to be general, and represents an important alterative to the use of oxoanion functional groups (PO_4^{3-}, SO_4^{2}, BO_3^{3-}, etc.) to achieve high discharge voltages.

Only the ordered polymorph of $Na(Ni_{2/3}Sb_{1/3})O_2$ exhibits the full theoretical capacity of 133 mAh/g. The maximum capacity of the disordered phase is 10 – 20 mAh/g lower both in our 1000 °C sample and in the 900 °C sample prepared by others. There are a variety of possible explanations for the reduced capacity of the disordered phase. The stacking faults may result in trapped regions of Na ions which have no diffusion pathway to the sample surface and are therefore inaccessible. It is also possible that the disordered structure is more susceptible to the loss of its immobile cations (Ni or Sb) to dissolution as non-ideal coordination environments will reduce the thermodynamic stability of these ions within the host framework. The present D-$Na(Ni_{2/3}Sb_{1/3})O_2$ phase exhibits a persistent difference in the observed charge and discharge capacities of 10 – 20 mAh/g. These differences in charge and discharge capacity are largest for the slowest charge/discharge rates, which are consistent with a small degree of self-discharge in these battery systems, an effect that could be attributed to inadvertent redox shuttles associated with dissolved Ni or Sb ions.

Phase changes during electrochemical cycling

A good understanding of the structural transitions associated with the electrochemical features of this system is important to understand the compact voltage profile exhibited by $Na(Ni_{2/3}Sb_{1/3})O_2$. The phase behavior of this system during electrochemical cycling was first probed through GITT measurements, in which a large relaxation time (30 hrs) was included between incremental charging steps in order to allow the true thermodynamic potential to be probed at different points in the charge/discharge response. This data is plotted as a function of state-of-charge in Fig. 11, while the same data is plotted as a function of time (so that it can be seen if full relaxation is achieved at each step) in Fig. S14. The GITT data for the ordered and disordered phases are qualitatively very similar, though in both cases the specific capacity should be treated as approximate due to the substantial influence of self-discharge processes over the timescale of these experiments (~1 month). Both the low voltage (~3.27 V) and high voltage (~3.64 V) plateaus are quite flat, with an observed deviation of less than 0.03 V from their average voltage over all of the points associated with these electrochemical features. This suggests that these plateaus are indeed associated with a two-phase reaction mechanism. Unfortunately, the step size of the GITT data does not allow good insights to be obtained about the phase behavior within the narrow intermediate voltage (3.3 – 3.6 V) regime between these two plateaus.

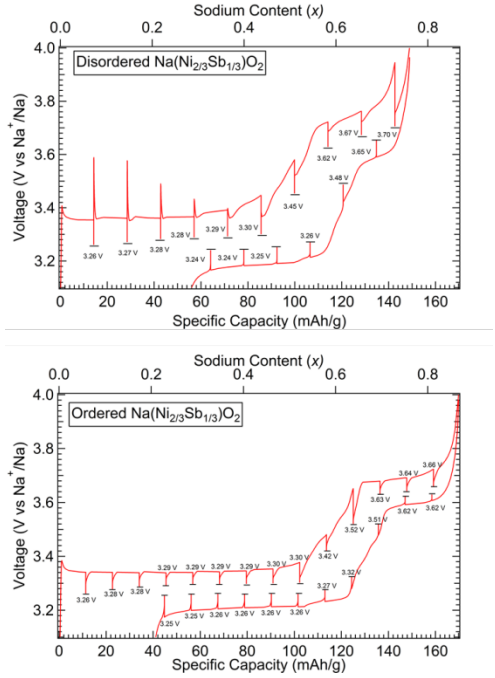

Figure 11. GITT of disordered (top) and ordered (bottom) $Na(Ni_{2/3}Sb_{1/3})O_2$ cycled between 2.5 and 4.0 V.

Complementary information about the phase evolution during cycling was obtained from *ex situ* synchrotron X-ray diffraction studies at a selection of points during the charge and discharge processes. The data for the disordered phase are presented in Fig. 12. It can be seen that during the 3.3 V charge plateau the system indeed behaves as expected for a two-phase reaction mechanism, as a new set of diffraction peaks appears and grows at the expense of the original O3-type $Na(Ni_{2/3}Sb_{1/3})O_2$ diffraction peaks. The new peaks can be indexed using a rhombohedral cell (*R3m*, #160), with lattice parameters of a = 2.96879(2) Å and c = 16.8862(2) Å in hexagonal setting. The *c*-lattice parameter is indicative of a 3-block repeat sequence (with each block having one layer of Na ions and one of Na/Sb cations) with an increased interblock spacing of 5.63 Å being relative to that of the pristine phase, as can be seen in the shift to higher angles of the peak at about 4.5 degrees 2θ associated with this *d*-spacing. In contrast, the *a*-lattice parameters are slightly reduced relative to the pristine phase as expected for the reduced Ni-O bond lengths that result from its oxidation.

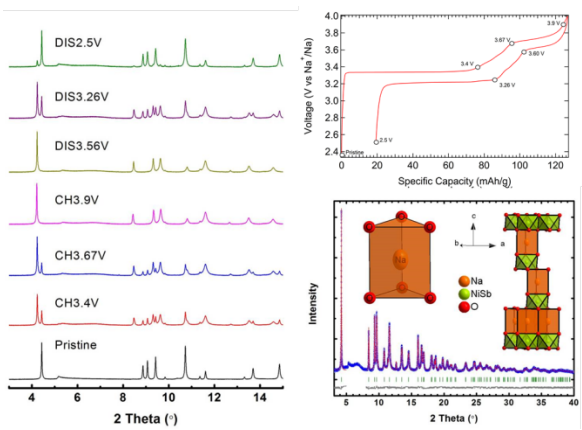

Figure 12. *Ex situ* synchrotron XRD patterns (left, λ = 0.41 Å) of disordered $Na(Ni_{2/3}Sb_{1/3})O_2$ collected on recovered cathodes of equivalent batteries cycled to different states of charge at the voltage points marked on a typical charge/discharge curve (Top right). One selected Rietveld refinement on the P3 phase formed after charging to 3.9 V (marked as CH3.9V) is shown in the bottom right panel, with the refined structure shown in inset (note large vertical axis of Na displacement parameter).

Rietveld refinements of these diffraction patterns suggest that the initial two-phase reaction corresponds to an O3 – P3 transition, which is known to occur in numerous other Na layered compounds[10, 33, 35]. This change in stacking sequence occurs when the Na ion coordination environments change to trigonal prismatic, and is in many cases driven by a reduction in Na content and typically results in increase in the interlayer spacing between transition metal layers. Refinements of the P3 phase associated with the disordered phase have been carried out in the space group of *R3m* (#160) that is commonly used to describe P3 type structure. A summary of the data collection parameters and the results of the crystallographic refinement are given in Tables S7–S9. When the corresponding X-ray data at the end of discharge are analyzed, it can be seen that O3 – P3 transition is reversible. A small amount of the P3 phase remains at the end of discharge, consistent with the observation that theoretical capacity of D-$Na(Ni_{2/3}Sb_{1/3})O_2$ is not fully realized even in the first discharge cycle.

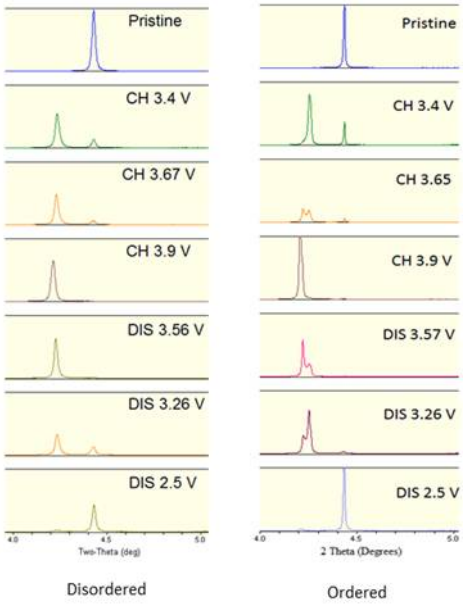

Figure 13. *Ex situ* synchrotron XRD patterns (λ = 0.41 Å) at low 2θ (between 4.0˚ and 5.0˚) of disordered (left) and ordered (right) $Na(Ni_{2/3}Sb_{1/3})O_2$ collected on recovered cathodes of equivalent batteries cycled to different states of charge/discharge.

The P3 stacking sequence that is present at the end of the first 3.3 V charge plateau appears to persist, as the major phase in the three XRD patterns collected at higher states of charge (CH3.67V, CH3.9V, DIS3.56V) appears visually indistinguishable from that observed at the end of the first charge plateau (CH3.4V). It is therefore concluded that the only major structural transition (involving layer shear and/or a change in the Na coordination environment) is the O3→P3 transition that occurs during the first charge plateau. The subsequent phase transitions are expected to be driven by minor variations in the Na site occupancies or the anisotropy of the transition metal containing octahedra resulting from electrochemical redox processes. The phase behavior of the ordered phase appears to be very similar to that of the disordered phase (Figure 13).

However, *ex situ* diffraction data collected near the beginning of the 3.6 V charge plateau (CH3.65, DIS3.57) now shows clear evidence for a two-phase mixture, which is interpreted as evidence for the co-existence of two distinct types of P3 stacking variants in these patterns. It is not known whether this observation represents a different structural progression for the ordered phase, or a more fortuitous choice of cutoff voltages, though the latter is judged more likely due to the very similar electrochemical response of the ordered and disordered phases.

The partially charged compositional endpoint of the 3.3 V charge plateau between pristine O3 $Na(Ni_{2/3}Sb_{1/3})O_2$ and the initial P3 phase is estimated to have the composition of $Na_{0.6}(Ni_{2/3}Sb_{1/3})O_2$ based on the specific capacity of ~80 mAh/g observed during the galvanostatic charging data of D-$Na(Ni_{2/3}Sb_{1/3})O_2$ samples. This suggests that the transition to the P3 phase requires the removal of almost half of the Na ions initially present in the structure. While the fully charged (CH3.9V) sample of disordered $Na(Ni_{2/3}Sb_{1/3})O_2$ may ideally be expected to have a composition of $Na_{1/3}(Ni_{2/3}Sb_{1/3})O_2$, the electrochemically determined capacity is expected to be closer to $Na_{0.4}(Ni_{2/3}Sb_{1/3})O_2$. However, both of these inferred stoichiometries have substantially less sodium than the composition determined by Rietveld refinement of the X-ray diffraction data for this phase, which is $Na_{0.7}(Ni_{2/3}Sb_{1/3})O_2$. It is often difficult to accurately refine the composition of atoms which are not well localized (due to the reduced scattering power from these sites whose periodicity is less coherent than sites with smaller average displacements), and an examination of the anisotropic displacement parameters of the Na site in this P3 structure type shows that they are indeed large, especially along the *c*-axis direction. In order to resolve this discrepancy, a larger (2 gram) sample of desodiated D-$Na(Ni_{2/3}Sb_{1/3})O_2$ was prepared by chemical oxidation using a solution of Br_2 in CH_3CN to enable time-of-flight neutron diffraction experiments on the POWGEN beamline. Neutron scattering occurs at the compact nucleus rather than in a diffuse electron cloud, and therefore the scattering power from atomic sites is better preserved at low *d*-spacings. As a result, Rietveld refinement of the neutron data (Fig. 14) is more sensitive to the Na occupancy. The composition refined from this data is $Na_{0.47}(Ni_{2/3}Sb_{1/3})O_2$, and is consistent with the electrochemical results. This demonstrates that it is unusually problematic to quantify the Na stoichiometry in this structure type by X-ray diffraction methods, likely due to the very large Na displacement parameters in the P3 trigonal prismatic sites.

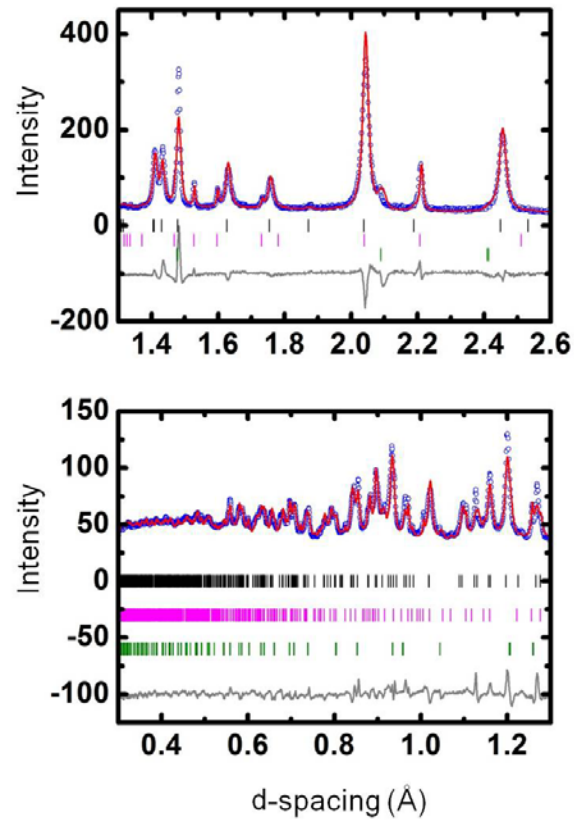

Figure 14. Rietveld refinement of time-of-flight neutron diffraction data for D-$Na_{0.47}(Ni_{2/3}Sb_{1/3})O_2$ obtained by chemical desodiation Black tick marks correspond to the desodiated P3 phase (~90 wt%), magenta to the pristine O3 phase (~7.5 wt%) and olive to a minor NiO impurity that was also present in the as-prepared material (~2.5 wt%).

The compositional endpoints of the O3-P3 phase transition appear to be sensitive to the synthesis conditions and the resulting concentrations of stacking faults. Based on electrochemistry of the disordered and ordered variants of $Na(Ni_{2/3}Sb_{1/3})O_2$ that are cycled at the same rate (C/50), the O3-P3 transition occurs at compositions of $Na_{0.6}(Ni_{2/3}Sb_{1/3})O_2$ and $Na_{0.5}(Ni_{2/3}Sb_{1/3})O_2$ for the disordered and ordered samples, respectively. Furthermore, others have reported that the O3-P3 transition occurs at a composition close to $Na_{0.67}(Ni_{2/3}Sb_{1/3})O_2$ in samples prepared at a lower temperature of 900 °C [22]. Taken together, these results indicate that the O3-P3 transition in $Na(Ni_{2/3}Sb_{1/3})O_2$ occurs earlier when a higher concentration of stacking faults are present. Interestingly, the end point of charging of 900 °C $Na(Ni_{2/3}Sb_{1/3})O_2$ to 4.0 V is reported to be an O1 phase[22] that is not observed in the present work, highlighting the sensitivity of the electrochemical response to the method of sample preparation and the extent of the long range ordering.

CONCLUSIONS

It is demonstrated that both "ordered" or "disordered" variants of $Na(Ni_{2/3}Sb_{1/3})O_2$ can be prepared by varying synthesis conditions. The combined Rietveld refinement of synchrotron and neutron diffraction data indicates that disordered D-$Na(Ni_{2/3}Sb_{1/3})O_2$ is best described by the $R\bar{3}m$ symmetry structure type of α-$NaFeO_2$. In contrast, a similar analysis unambiguously establishes that the ordered O-$Na(Ni_{2/3}Sb_{1/3})O_2$ structure has monoclinic *C2/m* symmetry, though its distortion from the ideal trigonal $P3_112$ symmetry is very small and cannot be easily resolved without utilizing high-resolution synchrotron data. It is found that the major difference between the "ordered" and "disordered" variants is the degree of coherence in the *c*-axis direction. Local structure studies show that both variants of this phase have a fully-developed honeycomb ordering of Ni and Sb cations. The disorder of D-$Na(Ni_{2/3}Sb_{1/3})O_2$ in the *c*-axis direction is associated with defects in the relative positions of the honeycomb lattices between successive layers. The electrochemical performance of ordered and disordered $Na(Ni_{2/3}Sb_{1/3})O_2$ is qualitatively similar, though only the ordered form exhibits the full 133 mAh/g theoretical capacity expected for the Ni^{3+}/Ni^{2+} redox couple. The dominant electrochemical response of both samples occurs in two electrochemical plateaus indicative of a two-phase reaction mechanism at 3.6 V (O3 → P3 transition) and 3.3 V (P3 → P'3 transition). These unusually high voltages are believed to be a consequence of Coulombic repulsions with the Sb^{5+} ions in the honeycomb lattice, and allow this system to deliver a very high energy density relative to alternative Na-ion battery systems.

ASSOCIATED CONTENT

Supporting Information

Diffraction, electrochemistry, electron microscopy and crystallographic data on the ordered and disordered $Na(Ni_{2/3}Sb_{1/3})O2$ phases. This material is available free of charge via the Internet at http://pubs.acs.org.

AUTHOR INFORMATION

Corresponding Author

cpg27@cam.ac.uk; kpete@bnl.gov

Author Contributions

† These authors contributed equally

ACKNOWLEDGMENT

This work was supported by the Northeastern Center for Chemical Energy Storage, an Energy Frontier Research Center funded by the U.S. Department of Energy, BES under award No. DE-SC0001294, including matching support from NYSTAR-NYSDED. Neutron scattering studies were supported by the Office of Basic Energy Sciences, U.S. Department of Energy, at the Spallation Neutron Source, Oak Ridge National Laboratory under contract DE-AC05-00OR22725 with UT Battelle. Dr. Joerg Neuefeind (NOMAD) and Dr. Pamela Whitfield (POWGEN) are acknowledged for their help in collection and processing of this data. Synchrotron XRD data was collected at the 11-BM beamline, and this use of the Advanced Photon Source (APS), an Office of Science User Facility operated for the U.S. Department of Energy, Office of Science, by Argonne National Laboratory, was supported by the US Department of Energy under contract No. DE-AC02-06CH11357. We thank R. Clément for stimulating discussion on the interpretation of NMR data, and J. Liu for assistance in SEM data collection, which were collected at Brookhaven National Laboratory's Center for Functional Nanomaterials supported by the DOE under grant DE-AC02-98CH10886.

REFERENCES

1. Armand, M.; Tarascon, J. M., Building better batteries. *Nature* **2008**, 451, 652-657.
2. Berthelot, R.; Carlier, D.; Delmas, C., Electrochemical investigation of the P2-Na_xCoO_2 phase diagram. *Nat. Mater.* **2011**, 10, 74-80.
3. Guignard, M.; Didier, C.; Darriet, J.; Bordet, P.; Elkaim, E.; Delmas, C., P2-Na_xVO_2 system as electrodes for batteries and electron-correlated materials. *Nat. Mater.* **2013**, 12, 74-80.
4. Liu, J.; Chang, D. H.; Whitfield, P.; Janssen, Y.; Yu, X. Q.; Zhou, Y. N.; Bai, J. M.; Ko, J.; Nam, K. W.; Wu, L. J.; Zhu, Y. M.; Feygenson, M.; Amatucci, G.; Van der Ven, A.; Yang, X. Q.; Khalifah, P., Ionic Conduction in Cubic $Na_3TiP_3O_9N$, a Secondary Na-Ion Battery Cathode with Extremely Low Volume Change. *Chem. Mater.* **2014**, 26, 3295-3305.
5. Ellis, B. L.; Nazar, L. F., Sodium and sodium-ion energy storage batteries. *Curr. Opin. Solid. St. M.* **2012**, 16, 168-177.
6. Palomares, V.; Casas-Cabanas, M.; Castillo-Martinez, E.; Han, M. H.; Rojo, T., Update on Na-based battery materials. A growing research path. *Energ. Environ. Sci.* **2013**, 6, 2312-2337.
7. Slater, M. D.; Kim, D.; Lee, E.; Johnson, C. S., Sodium-Ion Batteries. *Adv. Funct. Mater.* **2013**, 23, 947-958.
8. Kim, S. W.; Seo, D. H.; Ma, X. H.; Ceder, G.; Kang, K., Electrode Materials for Rechargeable Sodium-Ion Batteries: Potential Alternatives to Current Lithium-Ion Batteries. *Adv. Energy. Mater.* **2012**, 2, 710-721.
9. Kim, D.; Lee, E.; Slater, M.; Lu, W. Q.; Rood, S.; Johnson, C. S., Layered $Na[Ni_{1/3}Fe_{1/3}Mn_{1/3}]O_2$ cathodes for Na-ion battery application. *Electrochem. Commun.* **2012**, 18, 66-69.
10. Sathiya, M.; Hemalatha, K.; Ramesha, K.; Tarascon, J. M.; Prakash, A. S., Synthesis, Structure, and Electrochemical Properties of the Layered Sodium Insertion Cathode Material: $NaNi_{1/3}Mn_{1/3}Co_{1/3}O_2$. *Chem. Mater.* **2012**, 24, 1846-1853.
11. Buchholz, D.; Moretti, A.; Kloepsch, R.; Nowak, S.; Siozios, V.; Winter, M.; Passerini, S., Toward Na-ion Batteries-Synthesis and Characterization of a Novel High Capacity Na Ion Intercalation Material. *Chem. Mater.* **2013**, 25 , 142-148.
12. Yabuuchi, N.; Kajiyama, M.; Iwatate, J.; Nishikawa, H.; Hitomi, S.; Okuyama, R.; Usui, R.; Yamada, Y.; Komaba,

S., P2-type $Na_x[Fe_{1/2}Mn_{1/2}]O_2$ made from earth-abundant elements for rechargeable Na batteries. *Nat. Mater*. **2012**, 11, 512-517.

13. Padhi, A. K.; Nanjundaswamy, K. S.; Goodenough, J. B., Phospho-olivines as positive-electrode materials for rechargeable lithium batteries. *J. Electrochem. Soc.* **1997**, 144, 1188-1194.

14. Reynaud, M.; Ati, M.; Melot, B. C.; Sougrati, M. T.; Rousse, G.; Chotard, J. N.; Tarascon, J. M., $Li_2Fe(SO_4)_2$ as a 3.83 V positive electrode material. *Electrochem. Commun*. **2012**, 21, 77-80.

15. Bo, S. H.; Wang, F.; Janssen, Y.; Zeng, D. L.; Nam, K. W.; Xu, W. Q.; Du, L. S.; Graetz, J.; Yang, X. Q.; Zhu, Y. M.; Parise, J. B.; Grey, C. P.; Khalifah, P. G., Degradation and (de)lithiation processes in the high capacity battery material $LiFeBO_3$. *J. Mater. Chem.* 2012, **22**, 8799-8809.

16. Schmidt, W.; Berthelot, R.; Sleight, A. W.; Subramanian, M. A., Solid solution studies of layered honeycomb-ordered phases O3-$Na_3M_2SbO_6$ (M=Cu, Mg, Ni, Zn). *J. Solid. State. Chem.* **2013**, 201, 178-185.

17. Delmas, C.; Fouassier, C.; Hagenmuller, P., Structural Classification and Properties of the Layered Oxides. *Physica B & C* **1980**, 99, 81-85.

18. McQueen, T.; Huang, Q.; Lynn, J. W.; Berger, R. F.; Klimczuk, T.; Ueland, B. G.; Schiffer, P.; Cava, R. J., Magnetic structure and properties of the S=5/2 triangular antiferromagnet alpha-$NaFeO_2$. *Phys. Rev. B.* **2007**, 76,024420.

19. Dyer, L. D.; Borie, B. S.; Smith, G. P., Alkali Metal Nickel Oxides of the Type $MNiO_2$. *J. Am. Chem. Soc.* **1954**, 76, 1499-1503.

20. Politaev, V. V.; Nalbandyan, V. B.; Petrenko, A. A.; Shukaev, I. L.; Volotchaev, V. A.; Medvedev, B. S., Mixed oxides of sodium, antimony (5+) and divalent metals (Ni, Co, Zn or Mg). *J. Solid. State. Chem.* **2010**, 183, 684-691.

21. Ma, X. H.; Kang, K. S.; Ceder, G.; Meng, Y. S., Synthesis and electrochemical properties of layered $LiNi_{2/3}Sb_{1/3}O_2$. *J. Power. Sources*. **2007**, 173, 550-555.

22. Yuan, D.; Liang, X.; Wu, L.; Cao, Y.; Ai, X.; Feng, J.; Yang, H., A Honeycomb-Layered $Na_3Ni_2SbO_6$: A High-Rate and Cycle-Stable Cathode for Sodium-Ion Batteries. *Adv. Mater*. **2014**, DOI: 10.1002/adma.201401946.

23. Politaev, V. V.; Nalbandyan, V. B., Subsolidus phase relations, crystal chemistry and cation-transport properties of sodium iron antimony oxides. *Solid. State. Sci*. **2009**, 11, 144-150.

24. Strobel, P.; Lambertandron, B., Crystallographic and Magnetic-Structure of Li_2MnO_3. *J. Solid. State. Chem.* **1988**, 75, 90-98.

25. Massiot, D.; Fayon, F.; Capron, M.; King, I.; Le Calve, S.; Alonso, B.; Durand, J. O.; Bujoli, B.; Gan, Z. H.; Hoatson, G., Modeling one- and two-dimensional solid-state NMR spectra. *Magn. Reson. Chem*. **2002**, 40, 70-76.

26. Breger, J.; Jiang, M.; Dupre, N.; Meng, Y. S.; Shao-Horn, Y.; Ceder, G.; Grey, C. P., High-resolution X-ray diffraction, DIFFaX, NMR and first principles study of disorder in the Li_2MnO_3-$Li[Ni_{1/2}Mn_{1/2}]O_2$ solid solution. *J. Solid. State. Chem*. **2005**, 178, 2575-2585.

27. Barker, J.; Heap, R., Metallate electrodes. US Patent WO2013140174A3: 2013.

28. Vassilaras, P.; Ma, X. H.; Li, X.; Ceder, G., Electrochemical Properties of Monoclinic $NaNiO_2$. *J. Electrochem. Soc*. **2013**, 160, A207-A211.

29. Komaba, S.; Takei, C.; Nakayama, T.; Ogata, A.; Yabuuchi, N., Electrochemical intercalation activity of layered $NaCrO_2$ vs. $LiCrO_2$. *Electrochem. Commun.* **2010**, 12, 355-358.

30. Didier, C.; Guignard, M.; Denage, C.; Szajwaj, O.; Ito, S.; Saadoune, I.; Darriet, J.; Delmas, C., Electrochemical Na-Deintercalation from $NaVO_2$. *Electrochem. Solid. St.* **2011**, 14, A75-A78.

31. Ma, X. H.; Chen, H. L.; Ceder, G., Electrochemical Properties of Monoclinic $NaMnO_2$. *J. Electrochem. Soc.* **2011**, 158, A1307-A1312.

32. Zhao, J.; Zhao, L. W.; Dimov, N.; Okada, S.; Nishida, T., Electrochemical and Thermal Properties of alpha-$NaFeO_2$ Cathode for Na-Ion Batteries. *J. Electrochem. Soc*. **2013**, 160, A3077-A3081.

33. Delmas, C.; Braconnier, J. J.; Fouassier, C.; Hagenmuller, P., Electrochemical Intercalation of Sodium in Na_xCoO_2 Bronzes. *Solid State Ionics*. **1981**, 3-4, 165-169.

34. Kang, K. S.; Meng, Y. S.; Breger, J.; Grey, C. P.; Ceder, G., Electrodes with high power and high capacity for rechargeable lithium batteries. *Science* **2006,** *311*, 977-980.

35. Komaba, S.; Yabuuchi, N.; Nakayama, T.; Ogata, A.; Ishikawa, T.; Nakai, I., Study on the Reversible Electrode Reaction of $Na_{1-x}Ni_{0.5}Mn_{0.5}O_2$ for a Rechargeable Sodium-Ion Battery. *Inorg. Chem*. **2012**, 51, 6211-6220.

36. Gupta, A.; Mullins, C. B.; Goodenough, J. B., $Na_2Ni_2TeO_6$: Evaluation as a cathode for sodium battery. *J. Power Sources*. **2013**, 243, 817-821.